nature geoscience

ARTICLES

https://doi.org/10.1038/s41561-020-0578-1

Check for updates

The Earth's core as a reservoir of water

Yunguo Li[1]✉, Lidunka Vočadlo[1], Tao Sun[2] and John P. Brodholt[1,3]

Current estimates of the budget and distribution of water in the Earth have large uncertainties, most of which are due to the lack of information about the deep Earth. Recent studies suggest that the Earth could have gained a considerable amount of water during the early stages of its evolution from the hydrogen-rich solar nebula, and that a large amount of the water in the Earth may have partitioned into the core. Here we calculate the partitioning of water between iron and silicate melts at 20–135 GPa and 2,800–5,000 K, using ab initio molecular dynamics and thermodynamic integration techniques. Our results indicate a siderophile nature of water at core–mantle differentiation and core–mantle boundary conditions, which weakens with increasing temperature; nevertheless, we found that water always partitions strongly into the iron liquid under core-formation conditions for both reducing and oxidizing scenarios. The siderophile nature of water was also verified by an empirical-counting method that calculates the distribution of hydrogen in an equilibrated iron and silicate melt. We therefore conclude that the Earth's core may act as a large reservoir that contains most of the Earth's water. In addition to constraining the accretion models of volatile delivery, the findings may partially account for the low density of the Earth's core implied by measured seismic velocities.

Determining the water or hydrogen partition coefficient at high-pressure and high-temperature conditions between iron and silicate melts is not easy due to the low scatter cross-section area of hydrogen, and therefore various methods have been used to detect hydrogen indirectly. In 1996, Kuramoto and Matsui[1] estimated the partition coefficient of hydrogen between iron and silicate melts using a thermodynamic model based on gas solubility. They reported that hydrogen is siderophile and that the partitioning of hydrogen into iron increases with increasing pressure and temperature. A year later, Okuchi[2] measured the hydrogen partition coefficient by calculating the amount of hydrogen trapped in the bubbles of quenched FeH_x phases and determined the hydrogen concentration in the silicate melt through mass balance calculations. Their result agreed with the thermodynamic model in that over 95% of water accreted to the Earth should have reacted with iron and gone into the core. Several years later, Shibazaki et al.[3] employed a different method to determine the hydrogen partition coefficient between solid iron and ringwoodite, for which they estimated the hydrogen concentration in iron from hydrogenation-induced lattice expansion, and by Fourier transform infrared spectroscopy in ringwoodite. Their experiments also indicate the siderophile nature of hydrogen. In contrast, Zhang and Yin[4] reported an almost neutral behaviour of hydrogen between liquid iron and silicate melts at 3,200 K and 40 GPa by performing two-phase ab initio molecular dynamics (AIMD) simulations. Recently, Clesi et al.[5] used elastic recoil detection analysis to determine the hydrogen concentration in both iron and silicate melts at pressures of 5~20 GPa. They obtained a hydrogen metal–silicate partition coefficient of ~0.2, which indicates the lithophile behaviour of hydrogen. The contradiction with previous results was attributed to fugacity and possibly also to the presence of carbon in samples. Malavergne et al.[6] coupled the use of elastic recoil detection analysis and secondary ion mass spectrometry to measure the hydrogen partition coefficient. Their study confirmed the pressure effect on hydrogen partitioning observed before, and also suggest that hydrogen could change from lithophile to siderophile above ~15 GPa.

Free energy calculations

The discrepancies in the literature and the complexity of hydrogen partitioning hinder our further understanding of water in the Earth and necessitate a comprehensive study that can accurately describe the partitioning behaviour under various pressure, temperature and fugacity conditions. Ab initio thermodynamics is a reliable and widely used method for partition calculations under high-pressure–high-temperature conditions[7]. In this study, we calculated the Gibbs free energy of a series of iron and silicate melts with different concentrations of H_2/H_2O (Extended Data Fig. 1) by performing AIMD with thermodynamic integration. We considered two end-member systems: $P_{H_2O}/P_{H_2+H_2O} = 1$ and $P_{H_2}/P_{H_2+H_2O} = 1$ (namely, in the context of experiments, iron and silicate are equilibrated in the environment of pure H_2O or H_2 in these two cases), which represent oxidized and reduced conditions, respectively. The calculations were done at conditions above the solidus of our silicate melt at 20, 50, 90 and 135 GPa (ref. [8]), which correspond to temperatures of 2,800, 3,500, 3,900 and 4,200 K, respectively. We express the Gibbs free energy by $G(p,T,x) = \bar{G}(p,T,x) - TS_{mix}$, where x is the concentration of H or H_2O in iron or silicate melts, $\bar{G}$ is the pure component of Gibbs free energy and the term TS_{mix} is the entropy contribution from mixing. From the calculated Gibbs free energies, we derived the chemical potential of H/H_2O as $\mu_{H/H_2O}(p,T,x) = \bar{\mu}_{H/H_2O}(p,T,x) - TS_{mix}^{H/H_2O}$ (Methods). With the calculated chemical potentials $\mu_{H/H_2O}(p,T,x)$, the partition coefficients can be derived. Here, we use 'hydrogen' to refer to the general definition of 'water', and use H_2 and H_2O to denote the hydrogen and water molecules, respectively.

Figure 1a,b show our calculated Gibbs free energies $\bar{G}(p,T,x)$ of iron and silicate melts as a function of hydrogen concentration, and Fig. 1c,d plot the derived $\bar{\mu}_H$. Figure 1e–h show the Gibbs free energies $\bar{G}(p,T,x)$ of iron and silicate melts with H_2O and the derived pure component of chemical potential $\bar{\mu}_{H_2O}$. Under the same pressure, $\bar{\mu}_H$ is always lower in iron than in silicate. This is indicative that H is siderophile. Similarly, $\bar{\mu}_{H_2O}$ in liquid iron is

[1]Department of Earth Sciences, University College London, London, UK. [2]Key Laboratory of Computational Geodynamics, College of Earth and Planetary Sciences, University of Chinese Academy of Sciences, Beijing, China. [3]Centre for Earth Evolution and Dynamics, University of Oslo, Oslo, Norway. ✉e-mail: Yunguo.li@ucl.ac.uk

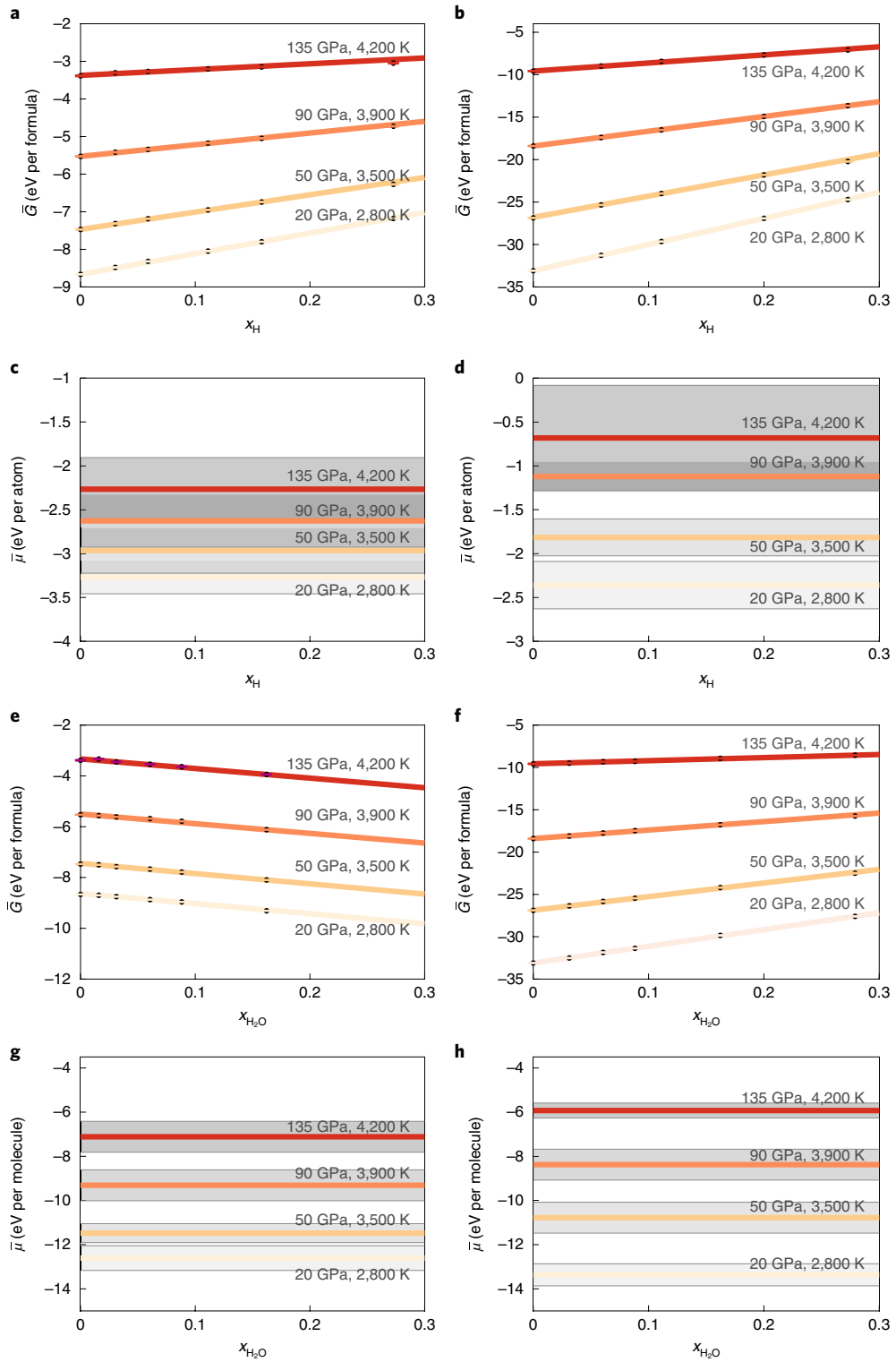

Fig. 1 | Calculated free energies. a,**b**,**e**,**f**, Calculated Gibbs free energies $\bar{G}(p, T, x)$ (points) and their fits (curves) for $Fe_{1-x}H_x$ (**a**), $(MgSiO_3)_{1-x}H_x$ (**b**), $Fe_{1-x}(H_2O)_x$ (**e**) and $(MgSiO_3)_{1-x}(H_2O)_x$ (**f**) melts, respectively. **c**,**d**,**g**,**h**, Derived $\bar{\mu}_{H/H_2O}(p, T, x)$ quantities in iron and silicate melts (H in Fe (**c**), H in $MgSiO_3$ (**d**), H_2O in Fe (**g**) and H_2O in $MgSiO_3$ (**h**)). Shaded regions indicate the uncertainties. See Extended Data Fig. 1 for the raw data and Supplementary Information for a better view with uncertainties.

also lower than that in silicate melt from 50 to 135 GPa (Fig. 1g,h,) which suggests a siderophile behaviour of H_2O; however, at 20 GPa, $\bar{\mu}_{H_2O}$ is slightly higher in liquid iron. This shows a pressure effect on H_2O partitioning.

Partitioning coefficients

With the obtained free energies, we calculated the partition coefficient of H between iron and silicate melts (denoted by $D_H^{Fe/MgSiO_3}$) by equating the chemical potentials of H ($\mu_H(p,T,x)$) in both iron and

silicate. As can be seen in Fig. 2a, $D_H^{Fe/MgSiO_3}$ does not show a visible dependence on x_H^{Fe}. $D_H^{Fe/MgSiO_3}$ is above 1 for all the examined pressures and compositions, which shows the siderophile nature of H. The calculated partition coefficient of H_2O between iron and silicate melts $D_{H_2O}^{Fe/MgSiO_3}$ is shown in Fig. 2b. Generally, H_2O is also siderophile except at 20 GPa, where H_2O is slightly lithophile. $D_{H_2O}^{Fe/MgSiO_3}$ shows a sharp increase approaching the concentration limit of $x_{H_2O}^{Fe}$, and such a behaviour is due to the entropy difference.

We did not include FeO in silicate melts nor O in the metal. The $MgSiO_3$ silicate is a good approximation to the lower mantle[9]. According to the estimated O budget in the outer core and FeO partition calculations[10], the content of FeO in liquid $MgSiO_3$ should not be appreciable. Furthermore, H atoms mainly pair with Fe and do not prefer an O–H bonding in liquid iron (Supplementary Information). Therefore, the presence of FeO in equilibrated iron and silicate melts will have negligible effects on the siderophile character of hydrogen. The presence of ferric iron in the silicate melt was also not considered as the amount of ferric iron present during core formation is likely to be very small[11]. However, regardless, the presence of ferric Fe_2O_3 should not also change the siderophile behaviour of hydrogen as Fe_2O_3 in the silicate melt would be subjected to the reaction $Fe_2O_3 + 2H = 2FeO + H_2O$, and this transformation (H to H_2O) basically does not change the siderophile nature of hydrogen.

We have also explored the temperature dependence of H partitioning at 135 GPa—conditions appropriate to the core–mantle boundary today. Gibbs free energies at temperatures from 4,200 to 5,000 K were obtained by integrating the Gibbs–Helmholtz equation based on the calculated temperature-dependent enthalpies (Extended Data Fig. 2) and assuming the same concentration dependence of Gibbs free energy to 4,200 K. As shown in Fig. 3, $D_H^{Fe/MgSiO_3}$ decreases with increasing temperature and is substantially lowered over the range from 4,200 to 5,000 K. By extrapolating our data, we found that the temperature would need to reach over ~6,500 K for H to become lithophile.

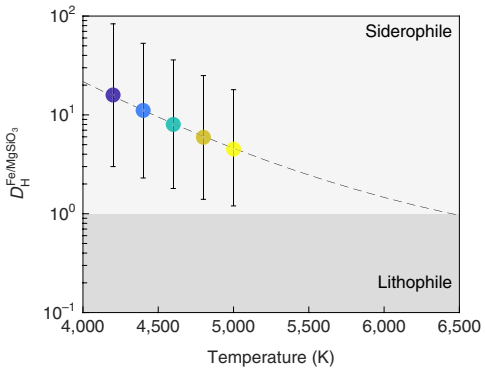

Fig. 3 | Temperature dependence of H partitioning. Calculated partition coefficient $D_H^{Fe/MgSiO_3}$ between iron and silicate melts as a function of temperature at 135 GPa. $D_H^{Fe/MgSiO_3}$ has little dependency on hydrogen concentration.

In addition to the free energy calculations, we performed another calculation using the empirical-counting strategy to verify the findings above (Methods). We built one supercell that contained a melt of 64 Fe atoms, a melt of 32 formula of $MgSiO_3$ and 12 H atoms sandwiched between the two melts; the system size was chosen to both minimize the surface area and maintain computational efficiency. The calculation was run at ~50 GPa and 3,500 K for 10 ps.

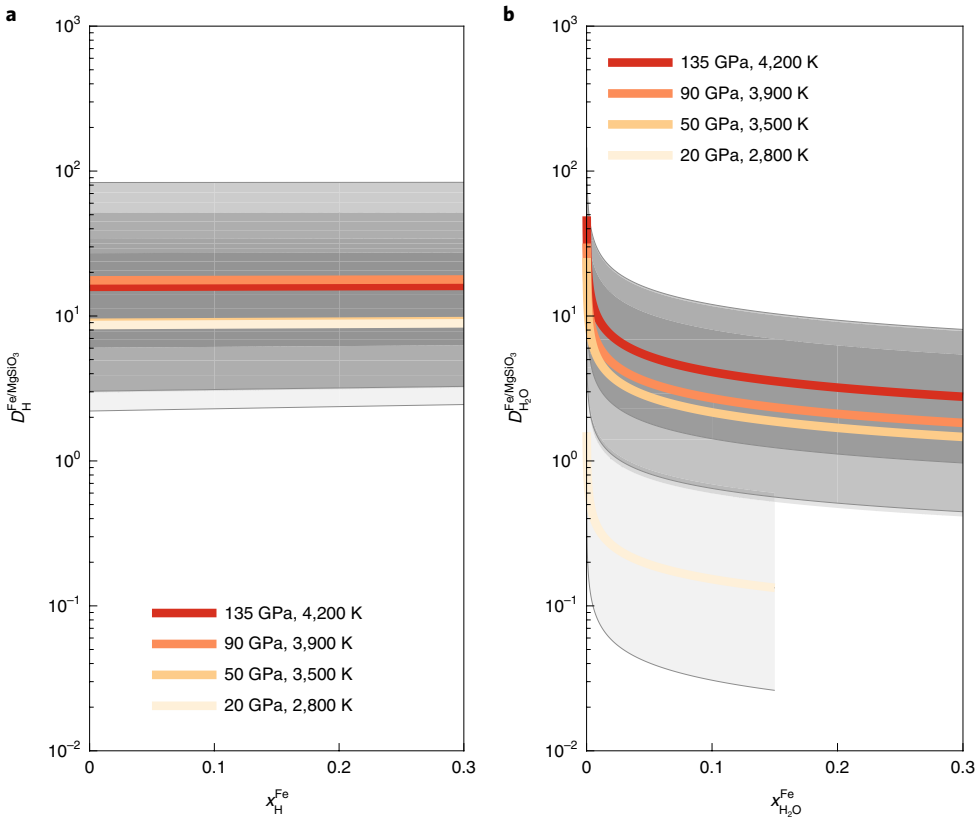

Fig. 2 | Partition coefficient. a,**b**, Derived partition coefficients between the iron and silicate melts as a function of concentration in iron for H (**a**) and H_2O (**b**). Shaded regions indicate the uncertainties. Supplementary Information gives a better view with uncertainties.

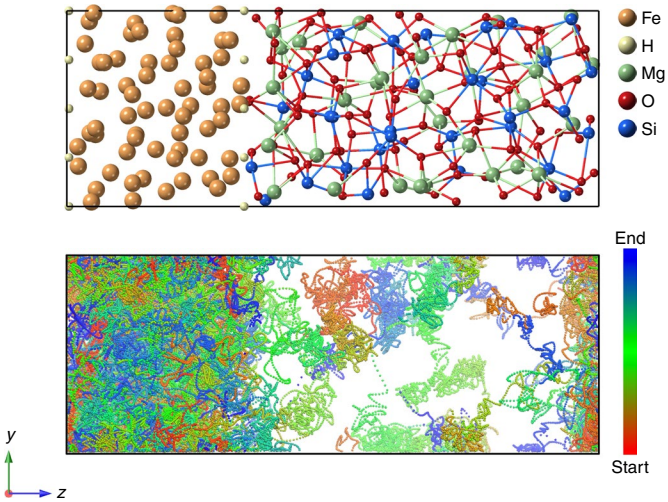

Fig. 4 | Empirical counting of H partitioning. Top panel: initial configuration of 12 hydrogen atoms sandwiched by 64 iron atoms and 32 formulae of $MgSiO_3$ for a NVT (constant number of atoms N, volume V and temperature T) run of 10 ps at ~50 GPa and 3,500 K. Both iron and silicate are in melt state during the calculation. Bottom panel: plot of the trajectories of the 12 hydrogen atoms.

Figure 4 shows the initial setting and AIMD trajectories (also see Supplementary Video 1). It can be seen that H atoms mostly reside in the Fe side during the run, which shows the siderophile nature of H. We counted the average number of H atoms at each side and obtained $D_H^{Fe/MgSiO_3} = 3.1 \pm 0.3$, which is lower than our free energy calculation result that gives $D_H^{Fe/MgSiO_3} = 9.1^{+18}_{-6}$. Note, however, that H diffuses much more slowly in silicate melt than in iron, so we might overcount the residence chance of H in the silicate and obtain a $D_H^{Fe/MgSiO_3}$ smaller than its true value. The data from empirical counting may be improved with a longer run, bigger supercells and multiple independent simulations. As well as H, some Si and O atoms also entered the iron region, which might also act to provide a slightly different $D_H^{Fe/MgSiO_3}$ compared with the free energy calculations. Nevertheless, these simulations agree qualitatively with the free energy results. Note that Zhang and Yin[4] obtained $D_H^{Fe/MgSiO_3} = 0.7 \pm 0.1$ using a similar two-phase model at 40 GPa and 3,200 K, which is lower than our value. The discrepancy is probably due to the setting of the two-phase model. They used a 44-iron atom cluster surrounded by silicate melt. Such a small cluster has a large surface-to-volume ratio and a substantial fraction of interface atoms, and so probably does not represent the true partitioning between the bulk phases.

Pressure and temperature dependence of water partitioning

In Fig. 5, we plot our partitioning coefficients of H and H_2O to compare with the literature values. Our results agree with the findings of Kuramoto and Matsui[1], Okuchi[2] and Shibazaki et al.[3], who determined the H concentration in iron via indirect methods. In contrast, Clesi et al.[5] and Malavergne et al.[6] found a more lithophile behaviour of hydrogen via direct methods. We note that the H concentration is high in Okuchi's[2] experiments ($x_H^{Fe} > 0.4$) and the experiments of Shibazaki et al.[3] ($x_H^{Fe} > 0.5$), and is low in the experiments of Clesi et al.[5] and Malavergne et al.[6] ($x_H^{Fe} < 0.03$). Our results show that H is always siderophile at all possible ranges, and the difference between experiments cannot be explained by the concentration difference. Experiments on the Fe–H system show that hydrogen is nearly insoluble in both solid and liquid iron below 1 GPa (refs. [12,13]), which suggests that the hydrogen that originally partitioned into iron at a high pressure may have escaped on depressurization, resulting in low concentrations in the Fe melt phase. In addition, Okuchi[2] found that there is a minimum $H_2O/MgSiO_3$ molar ratio ($m \geq 1.0$) needed to keep P_{H_2} in the experiment capsules, and in his experiments he used brucite, silicic acid and liquid H_2O to introduce hydrogen into the system. However, in the experiments of Clesi et al.[5] and Malavergne et al.[6], hydrogen was introduced into the system by adding $Al(OH)_3$ and brucite, and the $H_2O/MgSiO_3$ molar ratio was far less than that in Okuchi's experiments[2]. It is speculated that P_{H_2} is low in the experiments of Clesi et al.[5] and Malavergne et al.[6], and the actual condition could be more like our oxidizing case, $P_{H_2O}/P_{H_2+H_2O} = 1$. Their partition coefficients also match ours at oxidizing conditions.

Our H_2O partitioning coefficient strongly increases from 20 GPa to 50 GPa. The data of Clesi et al.[5] and Malavergne et al.[6] at more oxidizing conditions also show a similar trend from low pressures to ~20 GPa. Unfortunately, their data do not extend to 50 GPa and so cannot be used to confirm our high-pressure results, but the overlap at 20 GPa between our results and the experimental results is reassuring. As for the temperature effect, Kuramoto and Matsui's[1] result suggests that the increase of temperature strengthens the siderophile behaviour of H by using extrapolated temperature-dependent molar volumes and solubilities in their thermodynamic model. However, our free energy calculations clearly show the weakening of the siderophile behaviour with increasing temperature. We ran another empirical-counting simulation at ~50 GPa and 4,000 K and obtained $D_H^{Fe/MgSiO_3} = 2.1 \pm 0.3$, lower than that at ~50 GPa and 3,500 K. This confirms that $D_H^{Fe/MgSiO_3}$ decreases with increasing temperature. Apart from the pressure and temperature effects, there is a strong difference in the absolute value of hydrogen partitioning depending on whether it is H_2 or H_2O; nevertheless, both species show a siderophile behaviour at high pressures relevant to the core–mantle differentiation and core–mantle boundary conditions.

Water in the deep Earth

The calculated hydrogen partition coefficients imply that the Earth's core can potentially act as a large reservoir of water. How much water is in the core depends on the amount of water dissolved in the silicate melt during core formation, which is related to the Earth's accretion process, the mantle differentiation process and the extent of equilibrium. If we assume a homogeneous accretion model of water to the Earth and a single-stage core-forming process at 50 GPa and 3,500 K, over 76% of hydrogen will be partitioned into the core either at reducing conditions ($P_{H_2}/P_{H_2+H_2O} = 1$) or under oxidizing conditions ($P_{H_2O}/P_{H_2+H_2O} = 1$). This means that if the one ocean of water we see at the Earth's surface was degassed from the mantle during or just after core formation, then the core should contain a minimum of five oceans of water. Alternatively, in the case of a late veneer scenario, the Earth is almost free of water during the differentiation process and there would be hardly any water in the core.

Interestingly, our results show that at the current core–mantle boundary conditions, H_2 and H_2O are both more compatible in the core than in silicate melts. This means that any water held in a long-lived deep basal magma ocean[14] would tend to partition strongly into the core, which suggests that deep mantle anomalies resulting from a basal magma ocean (such as ultralow velocity zones and large low-shear-velocity provinces) should be relatively dry. In addition, any water added to the deepest mantle via subduction will also have a tendency to partition into the core now, either directly entering the core or reacting with liquid iron to form iron oxide and release H_2 into the core[15]. Regardless of which or any of these processes are occurring, the chemistry of the core should be subject to a constant change.

A recent model to explain the low D/H ratio of the Earth suggests a combination of chondritic water and ingassing of nebular hydrogen, with four-to-five oceans of water sequestered into the core[16].

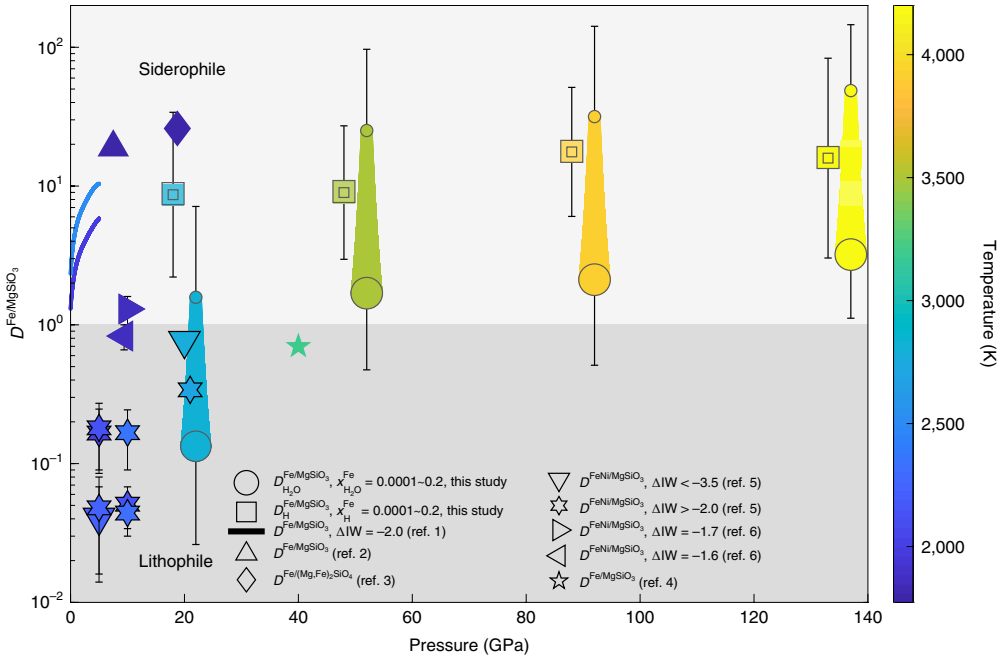

Fig. 5 | Comparison of partition coefficients with the literature. Compiled literature data in comparison with our partition coefficients of H and H_2O between iron and silicate melts calculated at 20, 50, 90 and 135 GPa, which correspond to 2,800, 3,500, 3,900 and 4,200 K. The partition coefficients of H and H_2O from this study are slightly shifted to lower and higher pressures, respectively, to facilitate a better view. The small and big squares (circles) indicate the partition coefficients of H (H_2O) at $x^{Fe}_{H/H_2O} = 0.0001$ and 0.2, respectively.

This was based on a high hydrogen solubility at high pressures and mantle hydrogen isotope fractionation. Our results are consistent with this model in that the core can be a reservoir of water. Recent noble gas isotope studies[17–19] and early-Earth ingassing modelling[20] also provide strong evidence for the capture of nebular hydrogen during Earth's accretion. According to our partitioning results, the core at present, therefore, could hold a substantial amount of water.

The presence of abundant hydrogen in the core may change its seismic, electric and thermal properties. Currently, core composition is still debated with an unexplained density deficit and low seismic velocities[21–23]. Umemoto and Hirose[24] show that ~1 wt% H in the outer core can match the compressional sound velocity and density, and suggest that hydrogen could be a primary light element in the core. A core with 1 wt% hydrogen is equivalent to the hydrogen content of ~130 oceans of water. Even with our highest partition coefficients at 50 GPa and 3,500 K, a core with that much water would result in a mantle content of some 23 oceans of water. With one ocean at the surface now, this implies that the current mantle should have 22 oceans of water, which is above even the most optimistic saturation limits for the mantle[25], unless bridgmanite is able to incorporate far more water than is currently expected[26]. Furthermore, hydrogen should also be able to partition into solid iron as the local environment of H in both solid and liquid iron is very similar, and the possibility of H in the inner core may also improve our current understanding about the inner core[27], for which only the multiple light elements model with carbon can explain its seismic properties[28].

Online content

Any methods, additional references, Nature Research reporting summaries, source data, extended data, supplementary information, acknowledgements, peer review information; details of author contributions and competing interests; and statements of data and code availability are available at https://doi.org/10.1038/s41561-020-0578-1.

Received: 8 November 2019; Accepted: 9 April 2020;
Published online: 18 May 2020

References

1. Kuramoto, K. & Matsui, T. Partitioning of H and C between the mantle and core during the core formation in the Earth: its implications for the atmospheric evolution and redox state of early mantle. *J. Geophys. Res. Planets* **101**, 14909–14932 (1996).
2. Okuchi, T. Hydrogen partitioning into molten iron at high pressure: implications for Earth's core. *Science* **278**, 1781–1784 (1997).
3. Shibazaki, Y., Ohtani, E., Terasaki, H., Suzuki, A. & Funakoshi, K. Hydrogen partitioning between iron and ringwoodite: implications for water transport into the Martian core. *Earth Planet. Sci. Lett.* **287**, 463–470 (2009).
4. Zhang, Y. & Yin, Q.-Z. Carbon and other light element contents in the Earth's core based on first-principles molecular dynamics. *Proc. Natl Acad. Sci. USA* **109**, 19579–19583 (2012).
5. Clesi, V. et al. Low hydrogen contents in the cores of terrestrial planets. *Sci. Adv.* **4**, e1701876 (2018).
6. Malavergne, V. et al. Experimental constraints on the fate of H and C during planetary core–mantle differentiation. Implications for the Earth. *Icarus* **321**, 473–485 (2019).
7. Alfè, D., de Wijs, G. A., Kresse, G. & Gillan, M. J. Recent developments in ab initio thermodynamics. *Int. J. Quantum Chem.* **77**, 871–879 (2000).
8. Stixrude, L. & Karki, B. Structure and freezing of $MgSiO_3$; liquid in Earth's lower mantle. *Science* **310**, 297–299 (2005).
9. Garnero, E. J., McNamara, A. K. & Shim, S.-H. Continent-sized anomalous zones with low seismic velocity at the base of Earth's mantle. *Nat. Geosci.* **9**, 481–489 (2016).
10. Pozzo, M., Davies, C., Gubbins, D. & Alfè, D. FeO content of Earth's liquid core. *Phys. Rev.* **9**, 041018 (2019).
11. Kaminsky, F. V. et al. Oxidation potential in the Earth's lower mantle as recorded by ferropericlase inclusions in diamond. *Earth Planet. Sci. Lett.* **417**, 49–56 (2015).
12. Fukai, Y., Mori, K. & Shinomiya, H. The phase diagram and superabundant vacancy formation in Fe–H alloys under high hydrogen pressures. *J. Alloys Compd* **348**, 105–109 (2003).
13. Fukai, Y. The iron–water reaction and the evolution of the Earth. *Nature* **308**, 174–175 (1984).
14. Labrosse, S., Hernlund, J. W. & Coltice, N. A crystallizing dense magma ocean at the base of the Earth's mantle. *Nature* **450**, 866–869 (2007).
15. Hu, Q. et al. FeO_2 and FeOOH under deep lower-mantle conditions and Earth's oxygen–hydrogen cycles. *Nature* **534**, 241–244 (2016).

16. Wu, J. et al. Origin of Earth's water: chondritic inheritance plus nebular ingassing and storage of hydrogen in the core. *J. Geophys. Res. Planets* **123**, 2691–2712 (2018).
17. Bouhifd, M. A., Jephcoat, A. P., Heber, V. S. & Kelley, S. P. Helium in Earth's early core. *Nat. Geosci.* **6**, 982–986 (2013).
18. Mukhopadhyay, S. & Parai, R. Noble gases: a record of Earth's evolution and mantle dynamics. *Annu. Rev. Earth Planet. Sci.* **47**, 389–419 (2019).
19. Williams, C. D. & Mukhopadhyay, S. Capture of nebular gases during Earth's accretion is preserved in deep-mantle neon. *Nature* **565**, 78–81 (2019).
20. Olson, P. & Sharp, Z. D. Hydrogen and helium ingassing during terrestrial planet accretion. *Earth Planet. Sci. Lett.* **498**, 418–426 (2018).
21. Tkalčić, H. & Pham, T. S. Shear properties of Earth's inner core constrained by a detection of *J* waves in global correlation wavefield. *Science* **362**, 329–332 (2018).
22. Hirose, K. et al. Crystallization of silicon dioxide and compositional evolution of the Earth's core. *Nature* **543**, 99–102 (2017).
23. Badro, J., Brodholt, J. P., Piet, H., Siebert, J. & Ryerson, F. J. Core formation and core composition from coupled geochemical and geophysical constraints. *Proc. Natl Acad. Sci. USA* **112**, 12310–12314 (2015).
24. Umemoto, K. & Hirose, K. Liquid iron-hydrogen alloys at outer core conditions by first-principles calculations. *Geophys. Res. Lett.* **42**, 7513–7520 (2015).
25. Nakagawa, T. & Iwamori, H. On the implications of the coupled evolution of the deep planetary interior and the presence of surface ocean water in hydrous mantle convection. *C.R. Geosci.* **351**, 197–208 (2019).
26. Hernández, E. R., Alfè, D. & Brodholt, J. The incorporation of water into lower-mantle perovskites: a first-principles study. *Earth Planet. Sci. Lett.* **364**, 37–43 (2013).
27. Militzer, B., Tagawa, S., Hirose, K. & Wahl, S. M. *Ab initio* simulations of hydrogen in the inner and outer core of the Earth. In *AGU Fall Meeting 2016* Abstr. MR22A-03 (AGU, 2016).
28. Li, Y., Vočadlo, L. & Brodholt, J. The elastic properties of hcp-Fe alloys under the conditions of the Earth's inner core. *Earth Planet. Sci. Lett.* **493**, 118–127 (2018).

Publisher's note Springer Nature remains neutral with regard to jurisdictional claims in published maps and institutional affiliations.

© The Author(s), under exclusive licence to Springer Nature Limited 2020

Methods

Chemical potential of H/H_2O. The chemical potential of H/H_2O in an iron/silicate melt, μ_{H/H_2O}, is the partial molar Gibbs free energy of H or H_2O:

$$\mu_{H/H_2O}(p,T,x)=\left(\frac{\partial G}{\partial n_{H/H_2O}}\right)_{p,T,n_{Fe/MgSiO_3}} \quad (1)$$

which is the free energy change when adding H or H_2O to the melts with all other conditions unchanged. We express the system Gibbs free energy by:

$$G(p,T,x)=\bar{G}(p,T,x)-TS_{mix} \quad (2)$$

where S_{mix} is the ideal mixing entropy, and $\bar{G}(p,T,x)$ is the pure component free energy and equal to the sum of the pure component of chemical potentials $\sum_{i=1}^{n}x_i\bar{\mu}_i$. The chemical potential also has two contributions, namely, the pure component and the mixing, and is written as

$$\mu(p,T,x)=\bar{\mu}(p,T,x)-TS_{mix} \quad (3)$$

We performed statistical tests on the calculated data $\bar{G}(p,T,x)$ per formula for the $Fe_{1-x}H_x$, $(MgSiO_3)_{1-x}H_x$, $Fe_{1-x}(H_2O)_x$ and $(MgSiO_3)_{1-x}(H_2O)_x$ systems, and the tests justify a linear model—the use of higher-order polynomials is statistically invalid. Therefore, we fitted the calculated $\bar{G}(p,T,x)$ with:

$$\bar{G}(p,T,x)=a+bx \quad (4)$$

where a and b are coefficients. We used a weighted fitting with the weight as $\left(\sum_{i=1}^{n}\sigma_{x_i}\right)/\sigma_{x_1}$, where x_i is the ith concentration and σ is the uncertainty of $\bar{G}$. $\bar{\mu}(p,T,x)$ for H and H_2O can be directly obtained, namely[10,29]:

$$\bar{\mu}_{H/H_2O}(p,T,x)=\bar{G}(p,T,x)+(1-x)\frac{\partial\bar{G}(p,T,x)}{\partial x}=a+b \quad (5)$$

The ideal mixing entropy for the $Fe_{1-x}H_x$, $(MgSiO_3)_{1-x}H_x$, $Fe_{1-x}(H_2O)_x$ and $(MgSiO_3)_{1-x}(H_2O)_x$ systems, respectively, are:

$$S_{mix}^{Fe_{1-x}H_x}=-k_BT[x\ln x+(1-x)\ln(1-x)] \quad (6)$$

$$S_{mix}^{(MgSiO_3)_{1-x}H_x}=-k_BT\left\{x\ln\left(\tfrac{x}{5-4x}\right)+(1-x)\left[2\ln\left(\tfrac{1-x}{5-4x}\right)+3\ln\left(\tfrac{3-3x}{5-4x}\right)\right]\right\} \quad (7)$$

$$S_{mix}^{Fe_{1-x}(H_2O)_x}=-k_BT\left\{x\left[2\ln\left(\frac{2x}{1+2x}\right)+\ln\left(\frac{x}{1+2x}\right)\right]+(1-x)\ln\left(\frac{1-x}{1+2x}\right)\right\} \quad (8)$$

$$S_{mix}^{(MgSiO_3)_{1-x}(H_2O)_x}=-k_BT\left\{\begin{array}{l}x\left[2\ln\left(\frac{2x}{5-2x}\right)+\ln\left(\frac{3-2x}{5-2x}\right)\right]\\+(1-x)\left[2\ln\left(\frac{1-x}{5-2x}\right)+3\ln\left(\frac{3-2x}{5-2x}\right)\right]\end{array}\right\} \quad (9)$$

k_B is the Boltzmann constant. Similarly, S_{mix}^{H/H_2O} can be calculated as $S_{mix}^{system}+(1-x)\frac{\partial S_{mix}^{system}}{\partial x}$. In equilibrium between the iron and silicate melts, the chemical potential $\mu_{H/H_2O}(p,T,x)$ in iron is equal to that in the silicate melt:

$$\begin{aligned}&\bar{\mu}_H^{Fe}(p,T,x)-T\left[S_{mix}^{Fe_{1-x}H_x}+(1-x)\tfrac{\partial S_{mix}^{Fe_{1-x}H_x}}{\partial x}\right]\\&=\bar{\mu}_H^{MgSiO_3}(p,T,y)-T\left[S_{mix}^{(MgSiO_3)_{1-y}H_y}+(1-y)\tfrac{\partial S_{mix}^{(MgSiO_3)_{1-y}H_y}}{\partial y}\right]\end{aligned} \quad (10)$$

$$\begin{aligned}&\bar{\mu}_{H_2O}^{Fe}(p,T,x)-T\left[S_{mix}^{Fe_{1-x}(H_2O)_x}+(1-x)\tfrac{\partial S_{mix}^{Fe_{1-x}(H_2O)_x}}{\partial x}\right]\\&=\bar{\mu}_{H_2O}^{MgSiO_3}(p,T,y)-T\left[S_{mix}^{(MgSiO_3)_{1-y}(H_2O)_y}+(1-y)\tfrac{\partial S_{mix}^{(MgSiO_3)_{1-y}(H_2O)_y}}{\partial y}\right]\end{aligned} \quad (11)$$

where y is the concentration of H/H_2O in silicate. At each x, we can obtain y and $D_{H/H_2O}^{Fe/MgSiO_3}=x/y$ by solving equations (10) and (11) analytically. Hence, the solute concentration in the silicate, $x_{H/H_2O}^{MgSiO_3}$, can be easily derived for each solute fraction in iron, x_{H/H_2O}^{Fe}, based on chemical potential functions, and the partition coefficient can also be determined.

AIMD. The Born–Oppenheimer AIMD calculations were performed with density functional theory. The projector augmented wave method[30,31] implemented in the VASP code[32,33] was employed to treat ion–electron interactions within the frozen-core approximation. Exchange-correlation effects were treated in the generalized gradient approximation parameterized by Perdew et al.[34]. The Fermi–Dirac statistics were used to populate single-particle orbitals. The plane-wave basis was generated with valence configurations of Fe $3p^63d^74s^1$, Mg $2p^63s^2$, Si $3s^23p^2$, O $2s^22p^4$ and H $1s^1$. There is a high-to-low spin transition in liquid iron, but the density difference between magnetic calculation and non-magnetic calculation at 20 GPa and 2,000 K is no more than 0.9% (ref. [35]), and magnetism mainly shifts the volume and/or pressure without bringing apparent structural changes[36]. The change to the chemical potential of H/H_2O by including magnetism is no more than 16/82 meV at 20 GPa. As discussed, the pressure effect on hydrogen partitioning is mainly due to the rapid increase in the hydrogen chemical potential in the silicate, which changes much more slowly in iron. Thus, to include magnetism basically does not change our conclusions and all the calculations were performed without spin polarization.

We modelled the iron melt with a supercell of 64 Fe atoms obtained by melting hexagonal close-packed Fe and used a supercell that contained 32 formulae of $MgSiO_3$ for the silicate melt obtained by melting perovskite. Then, we added H_2 or H_2O into the supercells. The examined compositions can be seen in Extended Data Fig. 1. Plane-wave energy cutoffs of 600 and 800 eV for the iron and silicate melts, respectively, were able to converge the energy within 1 meV per atom and pressure within 0.15 GPa together with a 2×2×2 Monkhorst–Pack k-mesh. To save computer time, we first ran the calculations using a single Gamma point and energy cutoffs of 400 and 600 eV for the iron and silicate melts, respectively. We then made corrections to 600 and 800 eV with a 2×2×2 Monkhorst–Pack k-mesh, respectively, by doing free energy perturbation and thermodynamic integration[37,38].

The iron and silicate melts were first relaxed at target pressures of 20, 50, 90 and 135 GPa, which correspond to temperatures of 2,800, 3,500, 3,900 and 4,200 K (roughly above the solidus of the silicate melt[8]). The relaxation was done with constrained NPT (constant number of atoms N, pressure P and temperature T) calculations that maintained the cubic supercell. A time step of 1 fs was used for all the NPT runs. The NPT calculations were run for over 10 ps and the lattice parameters were extracted from the final eight picoseconds. When shifted to different P–T conditions, the melt structures were allowed to relax long enough to approach the new P–T condition step-by-step. These derived lattice parameters were then used for NVT calculations, which normally last over several picoseconds; the first picoseconds were discarded for the free energy calculations.

Thermodynamic integration. Gibbs free energies of the melts were calculated by performing thermodynamic integration to the Weeks–Chandler–Andersen (WCA) gas system, which has established thermodynamics and no liquid–gas transition[39,40]. The efficiency of this approach was recently demonstrated in calculating the melting curve of elemental systems[37]. In this study, we extended this method to the free energy calculation of mixtures. The WCA system is a truncated repulsive Lennard–Jones system characterized by the energy parameter ε and length parameter σ, for which the potential ϕ_{WCA} is defined as:

$$\phi_{WCA}(r)=\left\{\begin{array}{c}4\varepsilon\left[\left(\frac{\sigma}{r}\right)^{12}-\left(\frac{\sigma}{r}\right)^{6}\right]+\varepsilon, r\le 2^{1/6}\sigma\\0, r>2^{1/6}\sigma\end{array}\right. \quad (12)$$

The potential during the transition from the ab initio system to the WCA system can be denoted as $\phi_\lambda=\phi_{WCA}+\lambda\phi$, where λ is the coupling parameter and ϕ is the electronic free energy from ab initio calculation. ϕ_λ smoothly shifts from the ab initio to the WCA potential as $\lambda\longrightarrow 0$ when we set $2^{1/6}\sigma$ to be less than the minimal bond length in the ab initio system. Gibbs free energy is calculated as $G=F(V)+P_0V$, where $F(V)$ is the Helmholtz free energy and P_0 is the target pressure. $F(V)$ can be determined via thermodynamic integration as:

$$F(V)=F_{WCA}+\frac{1}{N}\int_0^1\langle\phi_\lambda\rangle d\lambda=F_{WCA}+\frac{1}{Nm}\int_0^1\frac{\langle\phi_\lambda\rangle}{\lambda^{m-1}}d\lambda^m \quad (13)$$

where N is the number of atoms in the system and F_{WCA} is the documented free energy of the WCA gas[39,40]. We followed the previous study to transform λ to λ^m to ensure the integrand can be expressed in low-order polynomials[37]. A six-point Gaussian–Legendre quadrature was sufficient to converge the integral. F_{WCA} was calculated by $F_{WCA}=F_{ig}+F'_{WCA}$, where F_{ig} is the ideal gas free energy and F'_{WCA} is the free energy difference between the ideal gas and the WCA system, and:

$$F_{ig}=-k_BT\sum_{i=1}^{n}\ln Z_i=-k_BT\sum_{i=1}^{n}n\ln\left(\frac{\Omega}{N_i!\Lambda^{3N_i}}\right)=k_BT\sum_{i=1}^{n}\left(\ln\frac{\Lambda_i^3}{V}-1\right) \quad (14)$$

for the multicomponent system, where Ω is the system volume, V is the volume per atom, n is the number of elements and Z_i, N_i and Λ_i are the partition function, number of atoms and thermal wavelength, respectively, for element i. $\Lambda_i=h/\sqrt{2\pi m_ik_BT}$, where h is the Planck constant and m_i is the mass of element i.

The uncertainties in $\langle\phi_\lambda\rangle$ were obtained by using a blocking method and integrated to obtain the uncertainty of $\bar{G}$. The uncertainties of $\bar{\mu}_{H/H_2O}$ were derived following the error propagation rule.

Empirical-counting strategy. At 50 GPa and 3,500 K, we first relaxed both the iron (64 Fe atoms) and silicate (32 formulae of $MgSiO_3$) melt structures into a rectangular supercell with a square x–y plane of 9×9 Å^2. Then, we combined

the two supercells into one with some space between the two parts to place 12 hydrogen atoms. Six hydrogen atoms were inserted at each of the two Fe/$MgSiO_3$ interfaces. The integrated supercell was equilibrated within the NVT ensemble for 10 ps at 3,500 K. For each molecular dynamics step, we calculated the bond length for every hydrogen atom, which was tagged as a residence in the iron if its nearest neighbour atom is Fe apart from hydrogen. Finally, we obtained a partition coefficient $D_H^{Fe/MgSiO_3} = 3.1 \pm 0.3$.

Data availability

The raw outputs can be accessed in the UK National Geoscience Data Centre (NGDC) (https://doi.org/10.5285/d0677edf-c987-497d-aae8-23bf22ef774d). Any additional data can be requested by e-mailing the corresponding author.

Code availability

The Vienna Ab Initio Simulation Package is a proprietary software available for purchase at https://www.vasp.at/.

References

29. Li, Y., Vočadlo, L., Alfè, D. & Brodholt, J. Carbon partitioning between the Earth's inner and outer core. *J. Geophys. Res. Solid Earth* **124**, 12812–12824 (2019).
30. Kresse, G. & Furthmüller, J. Efficiency of ab-initio total energy calculations for metals and semiconductors using a plane-wave basis set. *Comput. Mater. Sci.* **6**, 15–50 (1996).
31. Kresse, G. & Hafner, J. *Ab initio* molecular dynamics for open-shell transition metals. *Phys. Rev. B* **48**, 13115–13118 (1993).
32. Kresse, G. & Joubert, D. From ultrasoft pseudopotentials to the projector augmented-wave method. *Phys. Rev. B* **59**, 1758–1775 (1999).
33. Blöchl, P. E. Projector augmented-wave method. *Phys. Rev. B* **50**, 17953–17979 (1994).
34. Perdew, J. P., Burke, K. & Ernzerhof, M. Generalized gradient approximation made simple. *Phys. Rev. Lett.* **77**, 3865–3868 (1996).
35. Edgington, A. L. *The Structure, Composition and Evolution of Mercury's Core* PhD thesis, Univ. College London (2016).
36. Prescher, C. et al. Structurally hidden magnetic transitions in Fe_3C at high pressures. *Phys. Rev. B* **85**, 140402 (2012).
37. Sun, T., Brodholt, J. P., Li, Y. & Vočadlo, L. Melting properties from *ab initio* free energy calculations: iron at the Earth's inner-core boundary. *Phys. Rev. B* **98**, 224301 (2018).
38. Vočadlo, L. & Alfè, D. *Ab initio* melting curve of the fcc phase of aluminum. *Phys. Rev. B* **65**, 214105 (2002).
39. Bharadwaj, A. S. & Singh, Y. Fluid–solid transition in simple systems using density functional theory. *J. Chem. Phys.* **143**, 124503 (2015).
40. Mirzaeinia, A., Feyzi, F. & Hashemianzadeh, S. M. Equation of state and Helmholtz free energy for the atomic system of the repulsive Lennard-Jones particle. *J. Chem. Phys.* **147**, 214503 (2017).

Acknowledgements

This work was supported by NERC grant NE/M015181/1 and NE/S01134X/1. We acknowledge the use of the NEXCS system, a collaborative facility supplied under the Joint Weather and Climate Research Program, a strategic partnership between the Met Office and the Natural Environment Research Council. This work also used the ARCHER UK National Supercomputing Service. T.S. acknowledges the Strategic Priority Research Program (B) of the Chinese Academy of Sciences (Grant no. XDB18000000).

Author contributions

Y.L. carried out the simulations and analysis. L.V. and J.P.B. supervised the project. All the authors contributed to the data analysis and writing the paper.

Competing interests

The authors declare no competing interests.

Additional information

Extended data is available for this paper at https://doi.org/10.1038/s41561-020-0578-1.

Supplementary information is available for this paper at https://doi.org/10.1038/s41561-020-0578-1.

Correspondence and requests for materials should be addressed to Y.L.

Peer review information Primary Handling Editor: Tamara Goldin.

Reprints and permissions information is available at www.nature.com/reprints.

P (GPa)	T (K)	Material	V (Å^3/atom)	$\bar{G}$ (eV/atom)	Material	V (Å^3/atom)	$\bar{G}$ (eV/atom)
20	2800	Fe_{64}	10.798	-8.665±0.008	$(MgSiO_3)_{32}$	9.984	-6.618±0.006
50	3500		9.999	-7.472±0.009		8.277	-5.373±0.008
90	3900		9.148	-5.527±0.011		7.281	-3.680±0.007
135	4200		8.509	-3.385±0.016		6.617	-1.915±0.008
20	2800	$Fe_{64}H_2$	10.578	-8.481±0.011	$(MgSiO_3)_{32}H_4$	9.763	-6.509±0.008
50	3500		9.751	-7.315±0.013		8.182	-5.267±0.008
90	3900		8.934	-5.416±0.014		7.199	-3.624±0.010
135	4200		8.312	-3.048±0.013		6.505	-1.850±0.010
20	2800	$Fe_{64}H_4$	10.372	-8.320±0.009	$(MgSiO_3)_{32}H_8$	9.639	-6.410±0.008
50	3500		9.544	-7.186±0.011		8.115	-5.191±0.009
90	3900		8.756	-5.342±0.013		7.089	-3.551±0.010
135	4200		8.125	-3.270±0.017		6.424	-1.826±0.010
20	2800	$Fe_{64}H_8$	9.936	-8.047±0.010	$(MgSiO_3)_{32}H_{12}$	9.522	-6.320±0.008
50	3500		9.132	-6.951±0.011		8.017	-5.174±0.009
90	3900		8.372	-5.175±0.013		6.986	-3.493±0.010
135	4200		7.766	-3.202±0.013		6.338	-1.814±0.010
20	2800	$Fe_{64}H_{12}$	9.557	-7.798±0.007	$(MgSiO_3)_{32}H_{24}$	9.272	-6.086±0.008
50	3500		8.776	-6.742±0.011		7.744	-4.900±0.009
90	3900		8.045	-5.048±0.013		6.743	-3.347±0.010
135	4200		7.449	-3.150±0.014		6.091	-1.783±0.010
20	2800	$Fe_{64}H_{24}$	8.662	-7.178±0.008	$(MgSiO_3)_{31}(H_2O)_1$	9.821	-6.584±0.008
50	3500		7.913	-6.271±0.011		8.210	-5.337±0.008
90	3900		7.222	-4.726±0.011		7.216	-3.667±0.011
135	4200		6.687	-3.048±0.013		6.539	-1.924±0.010
20	2800	$Fe_{62}(H_2O)_1$	10.515	-8.240±0.008	$(MgSiO_3)_{31}(H_2O)_2$	9.758	-6.528±0.008
50	3500		9.693	-7.127±0.014		8.155	-5.293±0.008
90	3900		8.880	-5.284±0.012		7.154	-3.637±0.008
135	4200		8.245	-3.246±0.014		6.483	-1.911±0.010
20	2800	$Fe_{62}(H_2O)_2$	10.263	-8.240±0.008	$(MgSiO_3)_{31}(H_2O)_3$	9.680	-6.503±0.007
50	3500		9.429	-7.127±0.014		8.072	-5.276±0.008
90	3900		8.640	-5.284±0.012		7.099	-3.621±0.008
135	4200		8.031	-3.246±0.014		6.437	-1.925±0.010
20	2800	$Fe_{62}(H_2O)_4$	9.799	-7.912±0.007	$(MgSiO_3)_{31}(H_2O)_6$	9.416	-6.383±0.010
50	3500		8.986	-6.840±0.012		7.894	-5.173±0.008
90	3900		8.202	-5.067±0.012		6.931	-3.587±0.010
135	4200		7.618	-3.158±0.014		6.270	-1.910±0.010
20	2800	$Fe_{62}(H_2O)_6$	9.380	-7.618±0.008	$(MgSiO_3)_{31}(H_2O)_{12}$	9.038	-6.212±0.010
50	3500		8.604	-6.619±0.013		7.570	-5.064±0.013
90	3900		7.846	-4.919±0.012		6.631	-3.543±0.010
135	4200		7.263	-3.092±0.013		6.002	-1.925±0.010
20	2800	$Fe_{62}(H_2O)_{12}$	8.513	-7.032±0.008	$(MgSiO_3)_{31}(H_2O)_{16}$		
50	3500		7.744	-6.114±0.012			
90	3900		7.021	-4.621±0.010			
135	4200		6.484	-2.978±0.013		5.841	-1.937±0.010

Extended Data Fig. 1 | Calculated free energies. Calculated volumes and Gibbs free energies $\bar{G}(p, T, x)$ of iron and silicate melts with H and H_2O at 20, 50, 90, and 135 GPa, corresponding to temperatures of 2800, 3500, 3900 and 4200 K, respectively.

Material	T (K)	V (Å^3/atom)	H (eV/atom)	$\bar{G}$ (eV/atom)
Fe_{64}	4200	8.509	1.150	-3.385
	4400	8.529	1.222	-3.603
	4600	8.568	1.313	-3.824
	4800	8.601	1.407	-4.050
	5000	8.627	1.497	-4.279
$Fe_{64}H_4$	4200	8.125	1.052	-3.270
	4400	8.162	1.122	-3.477
	4600	8.197	1.209	-3.688
	4800	8.219	1.307	-3.903
	5000	8.249	1.387	-4.122
$(MgSiO_3)_{32}$	4200	6.617	0.600	-1.915
	4400	6.642	0.684	-2.037
	4600	6.677	0.754	-2.162
	4800	6.687	0.868	-2.291
	5000	6.716	0.943	-2.424
$(MgSiO_3)_{32}H_8$	4200	6.424	0.641	-1.826
	4400	6.453	0.730	-1.946
	4600	6.473	0.794	-2.069
	4800	6.511	0.909	-2.196
	5000	6.534	0.972	-2.326

Extended Data Fig. 2 | Temperature dependence of free energies. Calculated volumes, enthalpies and Gibbs free energies $\bar{G}(p, T, x)$ of Fe_{64}, $Fe_{64}H_4$, $(MgSiO_3)_{32}$ and $(MgSiO_3)_{32}H_8$ at temperatures from 4200 to 5000 K under 135 GPa.